Mechanical properties of stromal striae, and their impact on corneal tissue behavior

Qian Wu, Chloé Giraudet, Jean-Marc Allain

journal of the mechanical behavior of biomedical materials 160 (2024) 106770

Contents lists available at ScienceDirect

Journal of the Mechanical Behavior of Biomedical Materials

journal homepage: www.elsevier.com/locate/jmbbm

Mechanical properties of stromal striae, and their impact on corneal tissue behavior

Qian Wu [a,b,*], Chloé Giraudet [a,b], Jean-Marc Allain [a,b,**]

[a] LMS, CNRS, Ecole Polytechnique, Institut Polytechnique de Paris, Palaiseau, France
[b] Inria, Palaiseau, France

ARTICLE INFO

Keywords:
Cornea
Stromal striae
DVC
OCT
Inflation

ABSTRACT

Cornea is an essential element of our eye. The refractive power of the cornea is closely related to its shape, which depends on the balance between its mechanical properties and the intraocular pressure. However, in keratoconus, the shape of the cornea is altered, and the mechanical properties (i.e., elastic modulus and viscosity) are reduced. These alterations have been associated with the development of striae within the cornea. Recently, such striae have been observed in healthy corneas as well, but with slightly different shapes. Our study investigated the mechanical role of these striae. To this end, we performed an inflation test under Optical Coherence Tomography: tomographic volumes were acquired in the central zone of eleven human corneas during an inflation test. Striae planes were extracted from the segmented images, and principal deformation maps were obtained by Digital Volume Correlation (DVC). We observe that the pattern of the striae does not change with pressure, even far above physiological pressure. Maximum principal strains are co-localized with the striae and are oriented perpendicular to the striae. We also observe that principal deformations on the striae increase with depth in the cornea. Our results show that striae lead to greater deformability in the direction perpendicular to the striae, especially in the posterior part of the cornea where they are the most visible. This supports the idea that the striae are undulations in the cornea collagenous microstructure, which are progressively unfolded under loading. They decrease the global stiffness of the cornea, in particular in the posterior part, and thus may help in accommodating deformations.

1. Introduction

Cornea, as the eye's outermost part, contributes to approximately two-thirds of the eye's refractive power (Ávila et al., 2019). The healthy human cornea is spherical-shaped, with an approximate thickness of 500 μm. However, in patients with certain conditions like keratoconus, the cornea becomes thinner and gradually bulges outward into an irregular cone shape, with steepening of the anterior and posterior corneal curvature. Such disease causes blurred or distorted vision.

Cornea is composed of five different layers: epithelium, Bowman's layer, stroma, Descemet's membrane, and endothelium. The stroma makes up approximately 90% of the total corneal thickness. The stroma is formed of lamellae a few micrometers thick, themselves formed of aligned and regularly spaced collagen fibrils. The lamellae are organized into a plywood-like structure. This very structured organization allows the transparency of the cornea (Maurice, 1957). The stroma is also thought to be responsible for corneal biomechanical stability (Montanino and Pandolfi, 2024). Weakened biomechanical properties are believed to cause steepening and thinning in keratoconic eyes (Giraudet et al., 2022; Padmanabhan et al., 2022).

In the posterior stroma, distinct lines known as stromal striae can be observed using imaging techniques (Grieve et al., 2017; Hollingsworth and Efron, 2005; Napoli et al., 2020). These striae cover approximately 50% of the stromal thickness, with an average width of 20 μm. Striae are frequently observed in patients with advanced keratoconus as vertical lines during classical clinical evaluation such as slit-lamp examination. It is reported that keratoconic eyes with more extended and more visible stromal striae have higher steepest corneal curvatures, thinner corneas, higher refractive errors, and lower biomechanical properties (Askarizadeh et al., 2017; Mocan et al., 2008; Rakhshandadi et al., 2021). These findings suggest that stromal striae may contribute to biomechanical deterioration in keratoconic eyes. The striae appear to be

* Corresponding author. LMS, CNRS, Ecole Polytechnique, Institut Polytechnique de Paris, Palaiseau, France.
** Corresponding author. LMS, CNRS, Ecole Polytechnique, Institut Polytechnique de Paris, Palaiseau, France.
E-mail addresses: qian.wu@polytechnique.edu (Q. Wu), jean-marc.allain@polytechnique.edu (J.-M. Allain).

https://doi.org/10.1016/j.jmbbm.2024.106770
Received 23 July 2024; Received in revised form 28 September 2024; Accepted 11 October 2024
Available online 12 October 2024

more prevalent with more powerful diagnostic techniques (Mocan et al. (2008)), such as confocal microscope. This has allowed to observe striae even in corneas without keratoconus (Grieve et al., 2017), with different morphologies: fewer, shorter and oblique. Our study aims at evaluating how the presence of stromal striae leads to local changes of mechanical response in healthy human cornea, which may further indicate the potential risk of striae to keratoconus.

To do so, we carried out inflation tests on ex-vivo healthy human corneas coupled with OCT imaging. The OCT images were further analyzed by Digital Volume Correlation (DVC) to characterize the corneal mechanical response at different pressures throughout the inflation test.

2. Materials and methods

Human tissues. This study was conducted in accordance with the principles outlined in the Declaration of Helsinki and adhered to international ethical standards for the use of human tissues. Handling of human corneas was duly reported to the French regulatory authority (CODECOH agreement DC-2019-3638). Eleven fresh and healthy corneas taken from human donors were assessed in our study. The donor corneas were provided by French Eye Bank (Banque Française des Yeux) after being deemed unsuitable for transplantation. Authorization for scientific research was granted by the donor families. The data of the corneas are gathered in Table 1. They were preserved in stem alpha 1 medium (Stem Alpha, France) during the first seven day, then stored in stem alpha 2 medium (Stem Alpha, France) for a maximum of 21 days. The corneas were then placed in stem alpha 3 medium (Stem Alpha, France) for deturgescence 48 h prior to the experiments.

Inflation test and ex-vivo imaging. Our protocol is similar to the one used in (Giraudet et al., 2024). The main elements are presented here. The cornea was placed on the top of an artificial anterior chamber, which was filled with physiological fluid stem alpha 3. A home-made injector is used to inject the fluid at a controlled rate. A pressure sensor (ATM.1 S T, STS, France) is placed next to the chamber (Moria, France): the pressure is measured every second. For all corneas, the pressure was initially increased incrementally in steps of 1.3–2 kPa (10–15 mmHg) up to 16 kPa (120 mmHg). For five of the corneas, only this first phase of the test was performed. For the remaining six corneas, the pressure was subsequently decreased back to physiological levels (2–2.7 kPa, 15–20 mmHg), before being increased again to 21 kPa (160 mmHg) (see Fig. 1). Each step lasted for 5 min, with the full test spanning a total of 155 min. Imaging was conducted after each pressure increment, with the injection paused to ensure static imaging conditions.

The chamber was placed under an Optical Coherence Tomograph (Ganymede-SP5, Thorlabs GmbH, Germany). Lacrigel Ophthalmic Gel (Laboratories EUROPHTA, Monaco) was placed between the OCT and the cornea to enable optical contact and maintain cornea hydration. 3D images were captured around the corneal apex using OCT at each pressure level, with a volume of 2.5 mm × 2.5 mm × 1.5 mm. The depth

Table 1
Data of the donor corneas.

Cornea Id	Age	Gender	Endothelial cell density (cell/mm^2)
1	72	F	1600
2	81	F	2650
3	66	M	2750
4	82	M	1950
5	87	F	2400
6	76	M	Impossible to count
7	58	M	1850
8	86	M	1700
9	82	M	1650
10	68	M	975
11	64	F	2650

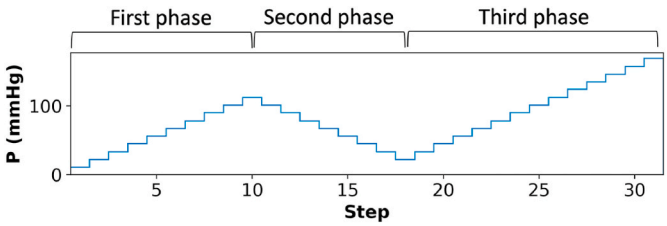

Fig. 1. Pressure steps during the full inflation test, including three phases.

dimension (1.5 mm) was calculated based on a refractive index of 1.33. The OCT system operated in A-scan mode with a scanning speed of 10 kHz. Lateral × depth resolution of the OCT was 4 μm × 2.5 μm in water. The pixel size in the in-plane directions was 6 μm, and 1.47 μm in the depth direction (for the refractive index of n = 1.33).

Striae segmentation. In each cornea, a boundary volume in posterior part containing the striae was extracted and segmented using Ilastik (Berg et al., 2019), a machine-learning-based image-analysis software. Initially, we conducted training to discern between striae and non-striae areas within select regions of the image. This training process uses feature criteria like pixel intensity and texture. Subsequently we applied this trained classification to the entire image, generating a probability map indicating the likelihood of each pixel being associated with striae. Then, we refined the object classification within the image based on additional features including intensity, location and shape. Using ImageJ, we further filtered the resulting probability map, creating a binary image where white pixels (gray level = 1) represented striae and black pixels (gray level = 0) represented non-striae areas. With the binary image established, we proceeded to detect striae planes and construct parametric models through point cloud processing techniques (Computer Vision Toolbox™ algorithms in MATLAB). Our approach consists in partitioning the range of [−360, 360] degrees into small intervals of 30° each. Within each interval, we applied the RANSAC algorithm over 10 iterations to fit a plan to the white pixels. After each iteration, the pixels that have been successfully fitted were excluded from consideration in subsequent iterations. This process was repeated for each interval, allowing us to identify all the striae planes in the 3D images (see Fig. 2).

Strain Measurement. The 3D OCT images were analyzed using the digital volume correlation software CMV3D, developed by Bornert et al. (2004), to obtain the displacement fields between the starting step (10–15 mmHg) and the ending step of the first phase (120 mmHg). The analysis utilized the contrast generated by microstructures (such as collagen lamellae and cells) to track regularly spaced points within a reference 3D volume. Each point was surrounded by a cubic correlation domain comprising 30^3 voxels. Intermediate steps were also analyzed to ensure better pattern tracking in the correlation process, especially given the significant changes between the images at the starting and ending step. After the correlation, a regular mesh whose nodes coincide with the centers of the correlation domains is constructed. The mesh and displacement field were used as inputs to compute strain tensors, in particular the maximum principal strain and its direction, via the finite element method implemented in the Python code myVTKPythonLibrary developed by Genet and Patte (2024). Since the deformation in the depth direction, likely controlled by osmotic effects and poroelastic behavior, is very dominant compared with the in-plane deformation under inflation test (Giraudet et al., 2024), in this study, the depth component was removed to consider only the maximum principal strain in the two-dimensional plane.

Statistic. The significance of image contrast difference between different pressure steps were assessed using the Wilcoxon test, chosen due to its robustness in analyzing small sample sizes. Pairwise test was used to compare the steps within each cornea independently. For the comparison of strain inside and outside striae, Student's t-test with equal variance was employed, preceded by a check of variance equality via

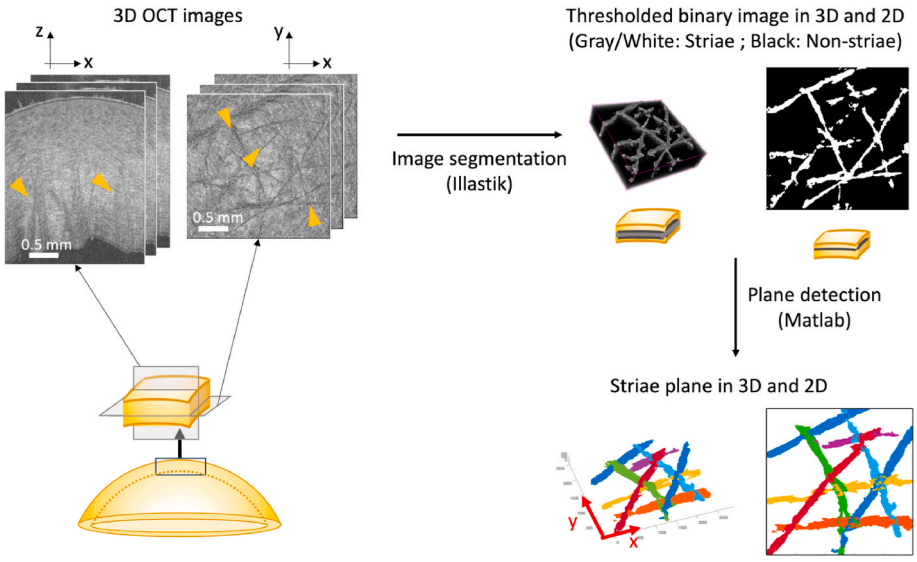

Fig. 2. Illustration of striae planes detection in 3D and on a 2D slice based on segmented binary images using point cloud processing techniques. The 3D OCT images were acquired by scanning a volume of the cornea near the apex. The volume was then segmented. Finally, the segmented striae were approximated by their fitting planes in the volume.

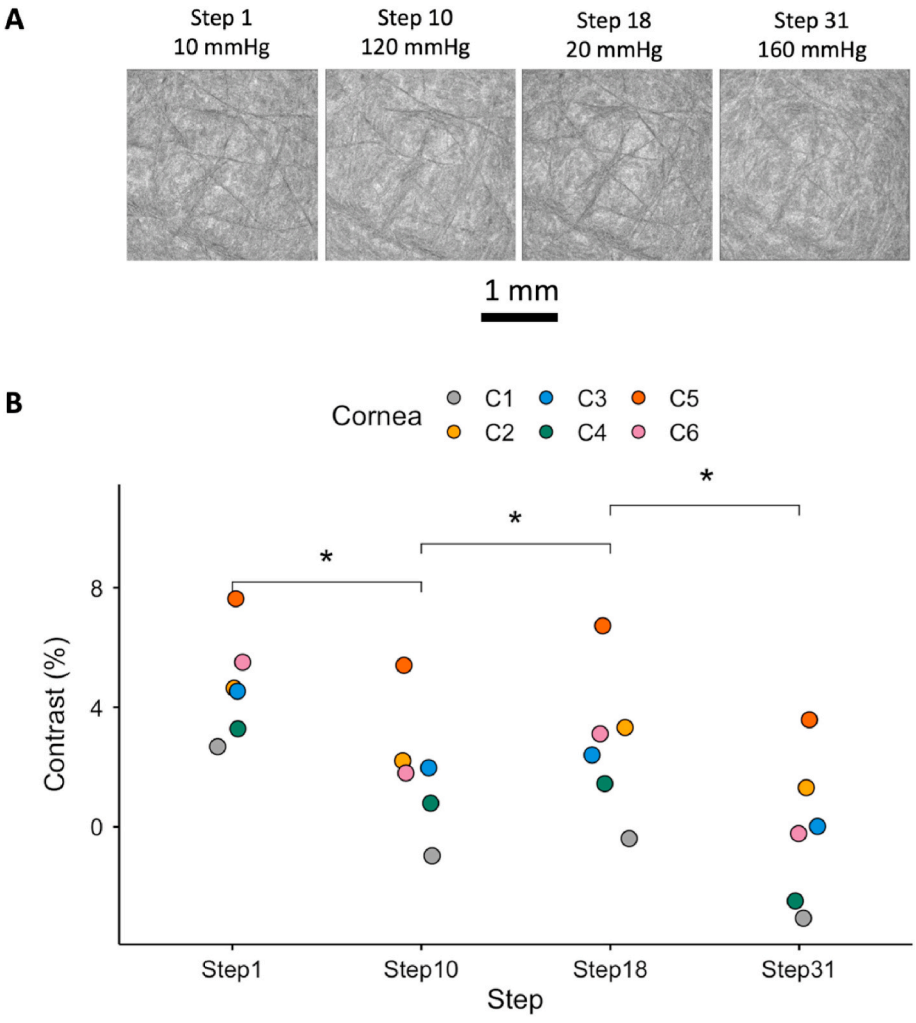

Fig. 3. **A**. In-plane OCT images taken at the same relative depth of the cornea C2 at different pressures. Steps 1, 10, 18 and 31 correspond respectively to the beginning and the end of the first phase, the end of the second phase, and the end of the third phase (see Fig. 1). **B**. Contrast levels indicating the visibility of striae in images from six corneas under different pressures. Contrast is determined by Eq. (1). Statistical analysis revealed significant pairwise differences between the steps, with $p = 0.03$.

Levene's test. Statistical tests were conducted using R. A difference was considered significant if the resulting p-value was less than 0.05. Results are reported as mean values ± standard deviation.

3. Results

The evolution of striae with pressure during a full inflation test is shown in Fig. 3. We show only the images taken at the maximum and minimum pressures. From in-plane OCT images taken at the same relative depth of the cornea and different pressures (see Fig. 3A), we observe that the pattern and position of the striae do not evolve with pressure throughout the inflation test. To quantify the visibility of striae areas, the contrast was determined as the difference between gray levels outside and inside striae normalized to the mean gray level:

$$Contrast = \frac{L_{out} - L_{in}}{L_{out} + L_{in}} \quad (1)$$

L_{in} and L_{out} being respectively the mean gray level inside and outside striae.

The calculated contrast of the six corneas indicates that the striae become less visible when the pressure increases (see Fig. 3B). But they do not disappear completely even at very high pressure (160 mmHg). Thanks to the stability of striae, we focused our analysis on the first phase (from Step 1 to Step 10) of the inflation test.

We wanted to know whether principal strains were significantly affected by the presence of striae. To achieve this, we separated the domains within the strain map into two groups based on the faction of striae pixels within each domain in the binary image: one group contained striae, while the other did not. A domain is considered to contain striae if half of its pixels are associated to striae after segmentation. Otherwise, it doesn't contain striae.

In Fig. 4A, we compare the OCT image of the cornea, the segmentation of striae, and the strain map at a particular depth for the maximal pressure value at the end of the first inflation. The striae seem colocalized with the higher principal strain. For a better quantification, we represented the distribution of normalized principal strains inside and outside striae across all depth levels and all the cornea samples (see Fig. 4B). The strain values of a given cornea were normalized by the mean principal strain within the entire analyzed volume of this cornea, i.e. within the depth range containing visible striae for each cornea. This normalization was needed to combine the results from different corneas, which have different mean strains for the same pressure. We observe that the principal strain inside the striae (2.1 ± 0.9) is in average twice that outside the striae (1.0 ± 0.7). A significant difference between the two groups is reflected in the statistical test by a $p < 0.0001$.

We then investigated the direction of the principal strain with respect to the striae orientation (see Fig. 5A). To do so, we selected only the domain containing striae, and computed the difference between the principal strain direction and the normal angle of the plane fitting the striae. Note that we used only the component of the angles within the plane of the OCT images, as we considered here only the in-plane strains. Fig. 5B shows the distribution of the difference of angle for all domains of all corneas. We adjusted the distribution by a Von Mises probability density function:

$$f(x \mid \mu, \kappa) = \frac{\exp[\kappa \cos(x - \mu)]}{2\pi I_0(\kappa)} \quad (2)$$

where $I_0(\kappa)$ is the modified Bessel function of the first kind and order zero (Cody, 1983), μ is the mean, κ is the concentration parameter. κ^{-1} described the spreading of the distribution, similar to variance in a Gaussian distribution. Our sample distribution is almost centered on 0 (mean: 0.06°), with a significant spreading ($\kappa^{-1} = 0.70$) (see Fig. 5B). We also quantified the link between the difference in angle and the principal strain at the same location (see Fig. 5C). The high principal strains exceeding 5% predominantly occur at small angles ([-30°, 30°]).

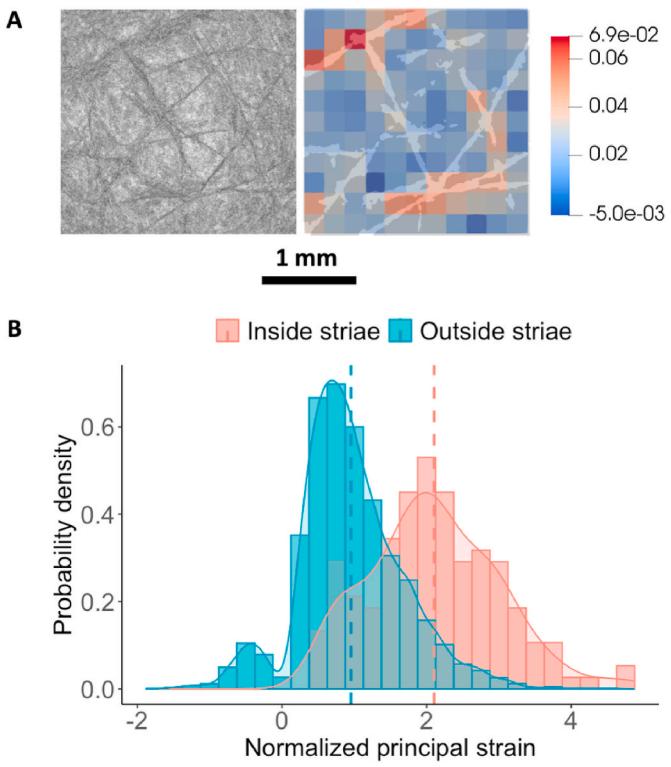

Fig. 4. A. (left) OCT image, and (right) the superposition of the segmented striae and the principal strain map, at a depth of 56% within the cornea C2, at the maximal pressure of the first inflation. Scale bar: 1 mm. **B.** Histogram of normalized principal strains inside and outside striae at all the depth levels and from all the cornea samples. The normalization is done by dividing the strain of a given cornea by the mean strain of this cornea, so that different corneas can be compared. The distribution inside striae is 2.1 ± 0.9, while outside striae it is 1.0 ± 0.7, showing a 55% change in the mean. A significance difference was observed with $p < 0.0001$.

Conversely, for low principal strains, the angle distribution extends over the entire range, although being also mainly occurring for small angles.

Although the striae are stable with pressure, we do not observe them through the full thickness of the tissue. They are visible on the deeper half of the cornea, as reported previously (Grieve et al., 2017), and more and more visible with depth. Thus, we decided to plot the mean principal strain at each depth from anterior (external) to posterior surface (see Fig. 6A). We separated the domain including striae (left) and without striae (right). As the striae are not visible through the full thickness, we extended the striae plane to the full thickness of the cornea: a domain that striae plane pass through is considered as being part of a stria. Otherwise, it is outside. We did this extension as our OCT has a limited resolution, and small striae may exist without being visible.

We observe an increase of the mean principal strains with depth in all corneas, within or outside striae. Moreover, we observe a stronger increase of the strain for domains including striae, but only in the half posterior part of the cornea. This observation is present in each cornea, as shown on Fig. 6B for 2 randomly chosen ones.

4. Discussion

The binary images segmented from Optical Coherent Tomography images allowed us to visualize the morphology of striae in the healthy corneas (see Fig. 2). From 2D slices, we can conclude that the striae are crisscrossing lines in front view and V-shape in cross section, which correspond to the structure in 3D image where the striae planes are roughly vertical but slightly oblique. This finding is consistent with the statement of Grieve et al. (2017) concerning healthy corneas. However,

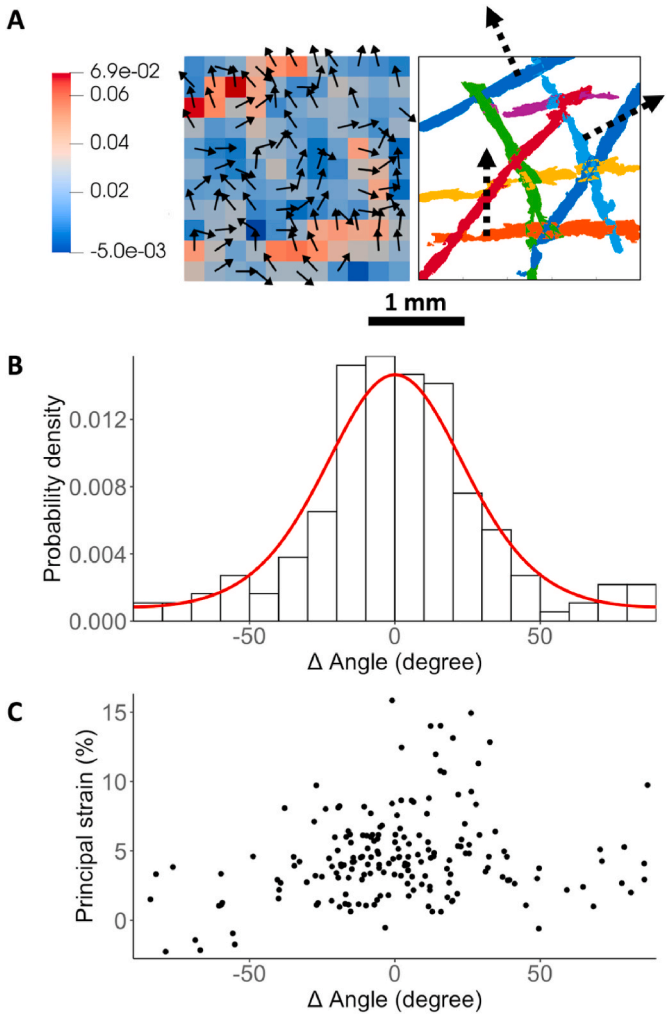

Fig. 5. A. Strain map with the directions of the maximum principal strains indicated by black arrows (left) and striae plane with their normal directions indicated by dashed black arrows (right). **B**. Probability density of Δ angle for all corneas at all depths. Red curve is the fitted Von-Mises distribution. **C**. Principal strain (in %) versus Δ angle for all domains including striae in all corneas.

the structure of striae in keratoconus seems different. Observed by several studies (Grieve et al., 2017; Krachmer, 1984; Mocan et al., 2008), the striae are parallels lines in front view and vertical in cross-section, and are usually aligned in the meridian of greatest curvature. Hollingsworth and Efron (2005) explained the orientation of the striae by stress patterns within the stroma. They suggested that the striae correspond to areas of reduced strength. Although the stromal striae can manifest in both normal and keratoconic eyes, the more severe disease the greater likelihood that striae will be present (Zadnik et al., 1996). In this study, we have focused on the biomechanics of healthy cornea. We observed first that the pattern of the striae is not affected by the pressure (see Fig. 3A), although the striae are less visible at very high pressure.

Our observations indicate that high deformation areas are co-localized with the striae (see Fig. 4), meaning that the striae are structures leading to a greater deformability. The highest principal deformation majorly occurs in the direction perpendicular to the striae plane (see Fig. 5). This indicates that the striae are strongly anisotropic structures, with large deformability only in the direction perpendicular to the structure. Our observations can be well explained by the idea that the striae are microstructural defects, such as undulations of collagen lamellae as described by Mocan et al. (2008) and Grieve et al. (2017). These undulations will be as stiff as the surrounding tissue in all directions, except the direction of the undulation where they will be much softer. Undulations explain also the decreasing contrast of the striae at high pressure (see Fig. 3B): the out-of-plane orientation of the undulated lamellae reduces the OCT signal, making the striae visible; the stretching of the tissue will flatten them, increasing the signal back-scattered from the striae. Thus, the striae contrast will decrease with stretching.

We then demonstrated that highest principal deformation is mainly perpendicular to the striae plane (see Fig. 5). This is more evident at high principal strain (>5%) than at low principal strain (<5%), where the data seem more affected by errors (see Fig. 5C). The large angle deviations at low principal strain can be firstly explained by the fitting process of striae plane. In fact, errors can be generated by the plane fitting function using random sample consensus algorithm. Each plane was described by a parametric model and included a 3D pixel cloud within tolerable distance and angular distance from the plane. A stria comprising small local irregularities oriented randomly may be approximately fitted to a plane. Consequently, the principal deformations at these local irregularities can occur at any other directions than the normal direction of the striae plane. Secondly, the experimental measures and the correlation process can also generate noise. However, this last noise was estimated to be lower than 1%.

In our study, we also observed that the cornea becomes more deformable at greater depth (see Fig. 6). This finding indicates that the cornea exhibits depth-dependent biomechanical properties, with the deeper regions being softer in the tangential direction than the anterior region. This is in agreement with other observations in the literature. Nambiar et al. (2023) demonstrated in a uniaxial traction test that the anterior cornea is the stiffest, with a stiffness 18% higher than that of the central cornea and 38% higher than that of the posterior layer. Dias and Ziebarth (2013) and Leonard et al. (2019) reported using AFM measurements that the elastic modulus of the anterior stroma was 3–7 times higher than that of the posterior stroma. Optical Coherence Elastography technique has also been employed to compare depth-resolved biomechanical properties (De Stefano et al., 2020), estimating an anterior-to-posterior stiffness ratio for the normal cornea of 1.135. Within anterior stroma, the growth trend of principal strain is the same inside and outside the striae planes. This can be explained by the fact that the striae are barely visible on the OCT images at this depth and the striae planes were obtained by extrapolation. Within posterior stroma, the increase of principal strain inside the striae is steeper than that outside the striae (see Fig. 6B): the striae allow for an additional softness, which becomes higher with depth. As the striae on the OCT image become also more and more visible with depth, one may consider that the softening comes from the larger and more pronounced undulation of the tissue, which itself can be associated with lower stretching resistance.

Finally, our results consistently indicate that the striae are undulations of the tissue, as also supported by microstructural observations (Raoux et al., 2023). However, the cause of these undulations remains unclear. One can propose two different origins: either the striae come from pre-existing structural defects of the collagen lamellae, or they are spontaneous folds of the tissue. In fact, both explanations may be applicable simultaneously, depending on the striae in question. The fact that the pattern and locations of the striae remain stable during the pressure evolution is insufficient to distinguish between the two explanations without further microstructural studies. SHG imaging of a normal cornea in the study of Grieve et al. (2017) showed the same tendency when the pressure changes between 0 mbar and 64 mbar. However, Krachmer et al. (1984) stated that the striae disappear with external pressure. The reason for this inconsistency between observations is unclear but may be related to the insufficient resolution of slit-lamp optics used in the study of Krachmer et al. It is also possible that *ex-vivo* specimens are more likely to be affected by spontaneous striae. Indeed, although we have taken all precautions to preserve the integrity of the cornea, the state of hydration of the *ex-vivo* specimen is different

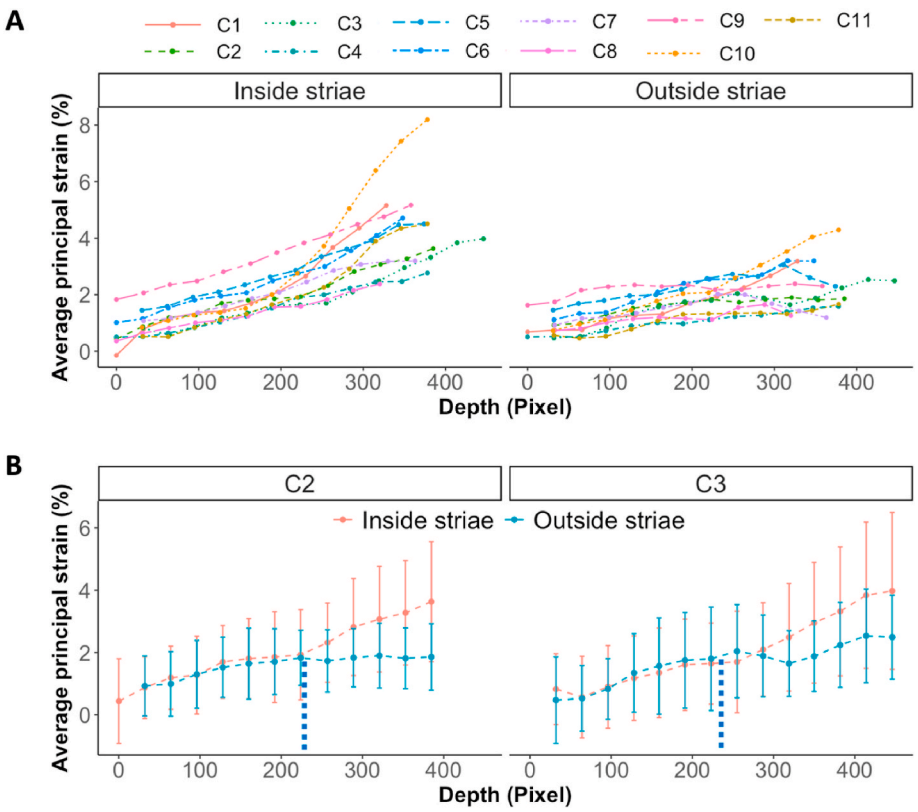

Fig. 6. A. Mean principal strain inside (left) and outside (right) striae plane as a function of depth in the central cornea for all samples. **B**. Comparison of mean principal strain inside and outside striae for 2 randomly chosen corneas. Error bars represent the dispersion of the strain at each depth. The blue dashed lines indicate depths above which striae were not visible. The pixel size in the depth direction is 1.47 μm (for refractive index of 1.33).

with that of *in-vivo* cornea. This results in slight undulations of the deeper part of the cornea, which increase the noise and decrease the striae contrast in the deeper stroma. More importantly, these undulations could lead to artificial striae by forcing the bending of the tissue.

To conclude, this study is a first step towards understanding the biomechanical role of the striae in normal cornea. We hypothesized that the striae have similar biomechanical role in pathological cornea, which could be confirmed in future experiment with keratoconus specimens. To go further, we will be interested in observing the behavior and structure of the striae more closely by using SHG (Second Harmonic Generation microscopy) and analysing the deformation around the striae on the scale of collagen lamellae. This may in particular allow us to test our hypothesis that the striae properties are coming from a microstructural undulation. Practically, this also means that stromal striae should be considered in the modelling of the entire stroma as a softening element.

CRediT authorship contribution statement

Qian Wu: Writing – original draft, Formal analysis. **Chloé Giraudet:** Writing – review & editing, Investigation. **Jean-Marc Allain:** Writing – review & editing, Supervision, Conceptualization.

Fundings

This work was supported by Agence Nationale de la Recherche (ANR-21-CE19-0010) and Ecole Polytechnique (interdisciplinary project METIS).

Declaration of competing interest

The authors declare that they have no known competing financial interests or personal relationships that could have appeared to influence the work reported in this paper.

Acknowledgments

The authors thank the Banque Française des Yeux (BFY, Paris) for providing human corneas, Vincent de Greef for his help in maintaining the inflation set-up, Hakim Gharbi and Simon Hallais for their help in the image correlation analysis, Poncia Nyembo, Gaël Latour, and Marie-Claire Schanne-Klein from LOB (IP Paris), and Vincent Borderie, from CHNO 15–20 (Inserm, Sorbonne University) for fruitful discussions.

Data availability

Data will be made available on request.

References

Askarizadeh, F., Sedaghat, M.-R., Ostadi-Moghaddam, H., Narooie, F., Rakhshandadi, T., Rajabi, S., 2017. A Contralateral Eye Study Comparing Corneal Biomechanics in Subjects with Bilateral Keratoconus with Unilateral Vogt's Striae.

Ávila, F.J., Gambín, A., Artal, P., Bueno, J.M., 2019. In vivo two-photon microscopy of the human eye. Sci. Rep. 9 (1), 10121. https://doi.org/10.1038/s41598-019-46568-z.

Berg, S., Kutra, D., Kroeger, T., Straehle, C.N., Kausler, B.X., Haubold, C., Schiegg, M., Ales, J., Beier, T., Rudy, M., Eren, K., Cervantes, J.I., Xu, B., Beuttenmueller, F., Wolny, A., Zhang, C., Koethe, U., Hamprecht, F.A., Kreshuk, A., 2019. ilastik: interactive machine learning for (bio)image analysis. Nat. Methods 16 (12), 1226–1232. https://doi.org/10.1038/s41592-019-0582-9.

Bornert, M., Chaix, J.-M., Doumalin, P., Dupré, J.-C., Fournel, T., Jeulin, D., Maire, É., Moreaud, M., Moulinec, H., 2004. Mesure tridimensionnelle de champs cinématiques par imagerie volumique pour l'analyse des matériaux et des structures.

Cody, W.J., 1983. Algorithm 597: sequence of modified Bessel functions of the first kind. ACM Trans. Math Software 9 (2), 242–245. https://doi.org/10.1145/357456.357462.

De Stefano, V.S., Ford, M.R., Seven, I., Dupps, W.J., 2020. Depth-dependent corneal biomechanical properties in normal and keratoconic subjects by optical coherence Elastography. Translational Vision Science & Technology 9 (7), 4. https://doi.org/10.1167/tvst.9.7.4.

Dias, J.M., Ziebarth, N.M., 2013. Anterior and posterior corneal stroma elasticity assessed using nanoindentation. Exp. Eye Res. 115, 41–46. https://doi.org/10.1016/j.exer.2013.06.004.

Genet, M., Patte, C., 2024. myVTKPythonLibrary. https://doi.org/10.5281/zenodo.11106508.

Giraudet, C., Diaz, J., Le Tallec, P., Allain, J.-M., 2022. Multiscale mechanical model based on patient-specific geometry: application to early keratoconus development. J. Mech. Behav. Biomed. Mater. 129, 105121. https://doi.org/10.1016/j.jmbbm.2022.105121.

Giraudet, C., Wu, Q., Allain, J.-M., 2024. Volumetric mechanical properties of soft tissues measured by optical coherence tomography: application to corneal heterogeneity. https://doi.org/10.2139/ssrn.4869831.

Grieve, K., Ghoubay, D., Georgeon, C., Latour, G., Nahas, A., Plamann, K., Crotti, C., Bocheux, R., Borderie, M., Nguyen, T.-M., Andreiuolo, F., Schanne-Klein, M.-C., Borderie, V., 2017. Stromal striae: a new insight into corneal physiology and mechanics. Sci. Rep. 7 (1), 13584. https://doi.org/10.1038/s41598-017-13194-6.

Hollingsworth, J.G., Efron, N., 2005. Observations of banding patterns (vogt striae) in keratoconus: a confocal microscopy study. Cornea 24 (2), 162–166. https://doi.org/10.1097/01.ico.0000141231.03225.d8.

Krachmer, J.H., 1984. Keratoconus and related noninflammatory Cornea1 thinning disorders. Surv. Ophthalmol.

Leonard, B.C., Cosert, K., Winkler, M., Marangakis, A., Thomasy, S.M., Murphy, C.J., Jester, J.V., Raghunathan, V.K., 2019. Stromal collagen arrangement correlates with stiffness of the canine cornea. Bioengineering 7 (1), 4. https://doi.org/10.3390/bioengineering7010004.

Maurice, D.M., 1957. The structure and transparency of the cornea. J. Physiol. 136 (2), 263–286. https://doi.org/10.1113/jphysiol.1957.sp005758.

Mocan, M.C., Yilmaz, P.T., Irkec, M., Orhan, M., 2008. The significance of Vogt's striae in keratoconus as evaluated by *in vivo* confocal microscopy. Clin. Exp. Ophthalmol. 36 (4), 329–334. https://doi.org/10.1111/j.1442-9071.2008.01737.x.

Montanino, A., Pandolfi, A., 2024. The inclusion of the epithelium in numerical models of the human cornea. Biomech. Model. Mechanobiol. 23 (3), 709–720. https://doi.org/10.1007/s10237-023-01801-7.

Nambiar, M.H., Seiler, T.G., Senti, S., Liechti, L., Müller, F., Studer, H., Roy, A.S., Büchler, P., 2023. Depth-dependent mechanical properties of the human cornea by uniaxial extension. Exp. Eye Res. 237, 109718. https://doi.org/10.1016/j.exer.2023.109718.

Napoli, P.E., Nioi, M., d'Aloja, E., Loy, F., Fossarello, M., 2020. The architecture of corneal stromal striae on optical coherence tomography and histology in an animal model and in humans. Sci. Rep. 10 (1), 19861. https://doi.org/10.1038/s41598-020-76963-w.

Padmanabhan, P., Lopes, B.T., Eliasy, A., Abass, A., Elsheikh, A., 2022. In vivo biomechanical changes associated with keratoconus progression. Curr. Eye Res. 47 (7), 982–986. https://doi.org/10.1080/02713683.2022.2058020.

Rakhshandadi, T., Sedaghat, M.-R., Askarizadeh, F., Momeni-Moghaddam, H., Khabazkhoob, M., Yekta, A., Narooie-Noori, F., 2021. Refractive characteristics of keratoconus eyes with corneal Vogt's striae: a contralateral eye study. Journal of Optometry 14 (2), 183–188. https://doi.org/10.1016/j.optom.2020.04.001.

Raoux, C., Chessel, A., Mahou, P., Latour, G., Schanne-Klein, M.-C., 2023. Unveiling the lamellar structure of the human cornea over its full thickness using polarization-resolved SHG microscopy. Light Sci. Appl. 12 (1), 190. https://doi.org/10.1038/s41377-023-01224-0.

Zadnik, K., Barr, J.T., Gordon, M.O., Edrington, T.B., 1996. Biomicroscopic signs and disease severity in keratoconus. Cornea 15 (2). https://journals.lww.com/corneajrnl/fulltext/1996/03000/biomicroscopic_signs_and_disease_severity_in.6.aspx.